Mode coupling and flow energy harvesting by a flapping foil

Qiang Zhu[a] and Zhangli Peng
Department of Structural Engineering, University of California, San Diego, La Jolla, California 92093, USA

(Received 22 September 2008; accepted 10 February 2009; published online 13 March 2009)

As demonstrated in recent studies, the bioinspired flapping foils are capable of harvesting kinetic energy from incoming wind or current. A practical measure to achieve this is via the coupling between different modes in a system with multiple degrees of freedom. A typical scenario includes external activation of one motion mode and extracting the mechanical energy from other modes that follow. In this study we create a numerical model based upon the Navier–Stokes equations to investigate the performance of such a system in low Reynolds numbers. The effects of both the mechanical design and the operational parameters are examined. Specifically, we concentrate on the vorticity control mechanisms involved in the process, and demonstrate that through vortex-body interactions energy of the leading-edge vortices can be partially recovered to enhance the energy harvesting capacity. © *2009 American Institute of Physics*. [DOI: 10.1063/1.3092484]

I. INTRODUCTION

Relying upon unsteady flow-body interactions for force generation, flapping foils are reminiscent of biological structures such as insect wings or fish fins. Through extensive experiments and theoretical/numerical investigations, these apparatuses have been shown to be highly efficient in producing thrust and maneuvering forces (see, e.g., Triantafyllou *et al.*[1] for a review).

In addition to their application as propellers, flapping foils are also capable of harvesting energy from vortices, free-surface waves, and uniform streams. The first case involves the foil's capacity of manipulating the ambient vorticity field as well as controlling its own vorticity shedding. For example, Gopalkrishnan *et al.*[2] experimentally studied the dynamics of a flapping foil within a vortex street generated upstream by a D-shape cylinder, and suggested that the foil might be able to enhance its thrust generation or propulsion efficiency through its interactions with the incoming vortices. At least two distinctive interaction modes were identified: the constructive mode and the destructive mode. In the constructive mode, the vortices created by the foil and the incoming vortex street are in the same phase and reinforce each other. It leads to stronger reverse Kármán vortex streets and increased thrust. The destructive mode, on the other hand, is characterized by a phase difference of approximately 180° between the foil-generated vortices and the incoming ones. As a result the combined wake is weakened, while the propulsion efficiency is increased. Similar vorticity control mechanisms have been discovered in interactions between leading-edge vortices (LEV) and trailing-edge vortices in a flapping foil,[3,4] or interactions between the vortices generated by the caudal fin and the dorsal/ventral fins of a fish during straight line swimming.[5] In addition, recent biomechanics studies illustrated that through the undulation of its body, a fish is capable of utilizing energy in upstream vortices to enhance its swimming performance.[6] Indeed, it was demonstrated that through passive body deformations and vorticity control, a fish could even propel itself forward inside a Kármán vortex street without energy expense (for numerical modeling see, e.g., Deng *et al.*,[7] Eldredge and Pisani[8]).

Closely related to these studies, the ability of a foil to extract energy from free-surface waves has also been reported. Isshiki *et al.*[9] and Grue *et al.*[10] experimentally and theoretically proved that a submerged foil, while deployed right beneath a free surface, is able to propel itself forward in both head and following sea conditions.

The basic idea to use a foil to harvest energy from a uniform flow was proposed over 2 decades ago.[11] Indeed, the capacity of the foil to absorb flow energy is clearly demonstrated in flow-induced vibrations such as flutter. To date there exist a handful of investigations about the energy harvesting potential of this device. In some previous studies, for example, the work by Jones and Platzer,[12] the energy exchange between a pitching/heaving foil and a uniform flow was examined and energy transfer from the flow to the foil was observed. Furthermore, it has been demonstrated that the amount of harvested energy could be increased by using two foils in tandem formation so that the downstream foil could recover energy from the wake of the upstream foil.[13] Following these, a recent numerical investigation was conducted by Dumas and Kinsey,[14] in which an energy harvesting efficiency of 34% was recorded when the pitching amplitude is over 55° [to put this in perspective, the theoretical limit of a flow kinetic energy harvesting device, commonly known as the Betz limit, is 0.59 (Ref. 15)]. In these studies, however, both the pitching and the heaving motions were prescribed so that the exact measures to activate these motions as well as the energy extraction mechanisms were not considered.

In fact, in existing designs the primary mechanism for a flapping foil to harvest energy from a uniform flow relies on the coupling of different motion modes and external activation is usually required. For example, for a foil capable of undergoing multi-degree-of-freedom motions (e.g., pitching and heaving), one of the modes (e.g., pitching) is actuated as

[a]Author to whom correspondence should be addressed. Electronic mail: qizhu@ucsd.edu. Telephone: +1-858-822-2161. Fax: +1-858-822-2260.

a periodic motion. Hydrodynamically, this produces periodic variations in the lifting and drag forces as well as pitching/rolling moments in an incoming flow. These time-varying forces/moments in their turn can trigger other modes (e.g., heaving), from which power extraction is achieved through attached generators. In recent years, this concept has attracted much attention owing to its potential application as tidal/current energy harvesting systems with low impact on the environment. The feasibility of such devices have been demonstrated in prototypes such as those developed by the Engineering Business and the BioPower Systems, dubbed Stingray and bioSTREAM™, respectively (see, e.g., Ref. 16).

In order to quantitatively predict the amount of flow energy that can be recovered by such a flapping-foil device and to identify key factors that may affect its performance, it is essential to resolve the coupling between different motion modes as determined by the hydrodynamic loading on the foil as well as the structural dynamics of the device itself. Shimuzu *et al.*[17] reported a two-dimensional Navier–Stokes simulation at Reynolds numbers of $O(10^5)$ in an attempt to identify optimal designs. Dynamic stall was found to be a possible mechanism of performance enhancement. However, no comprehensive investigation about the correlation between the near-body flow field and the energy harvesting capacity was conducted. In our previous work,[18] we studied the problem with a two-dimensional asymptotic model stemming from the thin-plate approximation by Theodorsen[19] and a three-dimensional boundary-element model.[5] To achieve simulations of fluid-structure interactions, both models were coupled with a spring-dashpot model representing effects of the power generator. The models were applied to map the energy harvesting capacity over a wide range of parameters, including the mechanical design of the system and the kinematic parameters related to its operation, and optimal conditions were identified. The primary drawback of this approach is that both models are based upon the potential-flow framework so that theoretically they are restricted to infinitely large Reynolds numbers. More importantly, in these potential-flow models the vorticity shed near the leading edge of the foil (leading-edge separation, or LES) is not incorporated. As illustrated by Anderson[3] and Anderson *et al.*,[4] LES contributes significantly to the dynamics of a flapping foil in cases with large frequencies or large effective angles of attack. On the other hand, as suggested by predictions made with our potential-flow models, large angles of attack often correlate with high energy recovery capacity (incidentally, this observation is consistent with the predictions by others, e.g., Dumas and Kinsey[14]). Clearly, it is critical to study dynamics of the system at large angels of attack with the effects of LES included.

We herein propose a Navier–Stokes model in which the fully viscous flow around a foil supported by a dashpot is solved. This model is then applied to simulate energy harvesting capacity of the foil in relatively low Reynolds numbers ($\sim$O(10^3)). It is therefore not our purpose in the current work to study performance of real systems under test (which are characterized by much larger Reynolds numbers). Rather, we will concentrate on the physical mechanisms that affect the mode coupling and subsequently the energy harvesting process of the system. Of particular interest is the effect of LES as well as interactions between LEV and the foil itself.

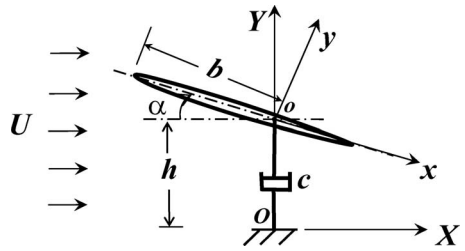

FIG. 1. Schematics of a flow energy harvesting system based upon a flapping foil.

The rest of this paper is organized as follows. In Sec. II we describe the physical problem, the mathematical model, and the numerical algorithm. It is followed by simulations showing dynamics of the system at different conditions and the underlying physical mechanisms. Finally, conclusions are drawn.

II. PROBLEM FORMULATION AND NUMERICAL METHODOLOGY

As shown in Fig. 1, we consider a two-dimensional foil with chord length a mounted on a damper c in an incoming flow U. The fluid density is ρ. The foil is allowed to undergo a heaving motion h and a pitching motion α around axis o. Through an actuating system, a sinusoidal pitching motion $\alpha(t)=\alpha_0 \cos(\Omega t)$ is activated. The heaving motion is then generated as $h=h(t)$. Assuming that the inertia of the foil is negligible (i.e., its own mass is much smaller than its added mass), the external torque required to actuate the pitching mode is $M_e=-M$, where M is the hydrodynamic pitching moment. Subsequently, the power input into the system is $P_i=M_e\dot{\alpha}=-M\dot{\alpha}$. The power output is obtained via the damper c, and expressed as $P_o=c\dot{h}^2$. The mean power input and output are defined as $\overline{P_i}=1/T\int_{t_0}^{t_0+T}P_i dt$ and $\overline{P_o}=1/T\int_{t_0}^{t_0+T}P_o dt$, respectively. Here $T=2\pi/\Omega$ is the period of the system. Finally, the net power output is given as $P=\overline{P_o}-\overline{P_i}$.

The performance of the system is also characterized by the power harvesting efficiency defined as the portion of flow energy flux within the swept area extracted by the device, i.e., $\eta=P/(1/2)\rho U^2 Y_p$ (where Y_p is calculated as the difference between the highest vertical position reached by the leading or trailing edges and the lowest vertical position). We note that this definition takes into account the effects of both the heaving and the pitching motions.

A. Mathematical formulations of fluid flow around the foil

In this study, we apply a two-dimensional Navier–Stokes model to solve the finite Reynolds number flow around a foil. The model is a modified version of the one reported by Guglielmini and Blondeaux.[20] In the following we summarize the primary steps of this approach.

The problem is formulated by using two Cartesian coordinate systems, a space-fixed coordinate system $(O-XY)$ and a body-fixed coordinate system $(o-xy)$ (Fig. 1). The transformation between the two systems is carried out by

$$\begin{bmatrix} x \\ y \end{bmatrix} = \begin{bmatrix} \cos\alpha & -\sin\alpha \\ \sin\alpha & \cos\alpha \end{bmatrix} \begin{bmatrix} X \\ Y-h \end{bmatrix}. \tag{1}$$

We assume that the foil has a Joukowski profile, which could be mapped into a circle with radius $\lambda+e+s$ in a (ξ,η) plane through the following transformation:

$$\mathbf{x} = \mathbf{z} + \frac{\lambda^2}{\mathbf{z}-e} + d - e, \tag{2}$$

where $\mathbf{x}=x+iy$ and $\mathbf{z}=\xi+i\eta$, $(i=\sqrt{-1})$. e and s are parameters characterizing the thickness of the foil and the sharpness of the trailing edge, respectively. d determines the location of the pitching axis o. Based on this formulation, the chord length a of the foil is $2(\lambda+e+s)+\lambda^2/(\lambda+s)+\lambda^2/(\lambda+2e+s)$, and $d=(\lambda+2e+s)+\lambda^2/(\lambda+2e+s)-b$, where b is the distance from the leading edge to the pitching point.

In the vorticity-stream function $(\omega-\psi)$ format, the Navier–Stokes equations are expressed as

$$\frac{\partial(J\omega)}{\partial t} + \sqrt{J}\mathbf{u}\cdot\nabla\omega = \frac{1}{R_{e\lambda}}\nabla^2\omega \tag{3}$$

and

$$\nabla^2\psi = -J\omega, \tag{4}$$

where $J=1+\{1-2[(\xi-e)^2-\eta^2]\}/[(\xi-e)^2+\eta^2]^2$ represents the Jacobian of the transformation $(\xi,\eta)\rightarrow(x,y)$. $\mathbf{u}$ is the flow velocity, $R_{e\lambda}=R_e\lambda/a$, where R_e is the Reynolds number based upon the chord length a and the incoming flow speed U.

For numerical purpose, within the (ξ,η) plane we define a cylindrical coordinate system (r,θ) with $r=\sqrt{\xi^2+\eta^2}$ and $\theta=\tan^{-1}(\eta/\xi)$. The Navier–Stokes equations (3) and (4) are thus rewritten in (r,θ) by using $\nabla=(\partial/\partial r,(1/r)(\partial/\partial\theta))$, $\nabla^2=(\partial^2/\partial r^2)+(1/r)(\partial/\partial r)+(1/r^2)(\partial^2/\partial\theta^2)$, and $\mathbf{u}=(u_r,u_\theta)$. The exact expression of these equations can be found in Guglielmini and Blondeaux.[20] We also have

$$u_r = \frac{1}{\sqrt{J}}\left[\frac{1}{r}\frac{\partial\psi}{\partial\theta} - (-\dot{h}\sin\alpha+\dot{\alpha}y)\left(\frac{\partial x}{\partial\xi}\cos\theta+\frac{\partial x}{\partial\eta}\sin\theta\right) - (\dot{h}\cos\alpha-\dot{\alpha}x)\left(\frac{\partial y}{\partial\xi}\cos\theta+\frac{\partial y}{\partial\eta}\sin\theta\right)\right], \tag{5}$$

$$u_\theta = \frac{1}{\sqrt{J}}\left[-\frac{\partial\psi}{\partial r} - (-\dot{h}\sin\alpha+\dot{\alpha}y)\left(-\frac{\partial x}{\partial\xi}\sin\theta+\frac{\partial x}{\partial\eta}\cos\theta\right) - (\dot{h}\cos\alpha-\dot{\alpha}x)\left(-\frac{\partial y}{\partial\xi}\sin\theta+\frac{\partial y}{\partial\eta}\cos\theta\right)\right]. \tag{6}$$

On the surface of the foil, we apply the no-flux and the no-slip boundary conditions so that the velocity components measured in the moving coordinate system disappear, i.e.,

$$u_r = 0, \tag{7}$$

$$u_\theta = 0. \tag{8}$$

Finally, we assume that in the far field $(r\rightarrow\infty)$ the flow field is undisturbed, thus

$$\frac{1}{r}\frac{\partial\psi}{\partial\theta} \rightarrow U\cos\alpha\left(-\frac{\partial y}{\partial\xi}\sin\theta+\frac{\partial y}{\partial\eta}\cos\theta\right) + U\sin\alpha\left(\frac{\partial x}{\partial\xi}\sin\theta-\frac{\partial x}{\partial\eta}\cos\theta\right), \tag{9}$$

$$\frac{\partial\psi}{\partial r} \rightarrow U\cos\alpha\left(\frac{\partial y}{\partial\xi}\cos\theta+\frac{\partial y}{\partial\eta}\sin\theta\right) + U\sin\alpha\left(-\frac{\partial x}{\partial\xi}\cos\theta+\frac{\partial x}{\partial\eta}\sin\theta\right), \tag{10}$$

and

$$\omega = 0. \tag{11}$$

B. Hydrodynamic forces and moments

Based upon the vorticity field, the hydrodynamic force on the foil is conveniently determined (see, e.g., Ref. 21), and expressed as

$$\mathbf{F} = \mu\oint_{S_b}\left[(\mathbf{X}-\mathbf{X}_o)\times\frac{\partial\boldsymbol{\omega}}{\partial n} - \mathbf{n}\times\boldsymbol{\omega}\right]ds + \rho A\ddot{h}\mathbf{e}_Y, \tag{12}$$

where $\boldsymbol{\omega}=\omega\mathbf{e}_Z$. $\mathbf{n}$ is the unit surface normal vector pointing into the fluid. $\mathbf{X}_o$ is the location of the pitching axis. A is the area of the body. μ and ρ are the dynamic viscosity and the density of the fluid, respectively. The integration is performed around the body surface S_b.

Similarly, the hydrodynamic moment with respect to the pitching axis is obtained as

$$M = \mu\oint_{S_b}(\mathbf{X}-\mathbf{X}_o)\times\left[\frac{1}{2}(\mathbf{X}-\mathbf{X}_o)\times\frac{\partial\boldsymbol{\omega}}{\partial n} - \mathbf{n}\times\boldsymbol{\omega}\right]\cdot\mathbf{e}_Z ds + 4\mu A\dot{\alpha} - \rho\ddot{\alpha}(A|\mathbf{X}-\mathbf{X}_o|^2+2B) + \rho A\ddot{h}\mathbf{e}_Z\cdot[(\mathbf{X}-\mathbf{X}_o)\times\mathbf{e}_Y], \tag{13}$$

where B is the second area moment of inertia of the body. $\mathbf{e}_Y$ and $\mathbf{e}_Z$ are the unit vectors in the Y and Z (pointing out of the plane) directions, respectively.

The lifting and the drag forces, i.e., the Y and X components of $\mathbf{F}$, are F_L and F_D. The lifting and the drag coefficients are defined as $C_L=F_L/(1/2)\rho U^2 a$ and $C_D=F_D/(1/2)\rho U^2 a$, respectively.

By assuming that the inertia of the foil is negligible compared to its added mass, the heaving motion of the foil is determined by the lifting force F_L and the damper c, i.e.,

$$\dot{h} = F_L/c. \tag{14}$$

C. Numerical issues

We discretize the Navier–Stokes equations (3) and (4) in r, θ, and t. Following Guglielmini and Blondeaux,[20] to increase the resolution near the foil surface and account for the boundary-layer effect, we define a new variable $z=ln(r+r_0)$ and apply N_r evenly distributed grids along z. The parameter r_0 can be adjusted so that the sizes of the grids close to the foil surface are much smaller than the boundary-layer thickness to maintain sufficient resolution.[22] The outer boundary is about eight chord lengths away from the body. Sensitivity tests have been conducted to make sure that the results are not significantly affected by the size of the computational domain. In the θ direction, N_θ evenly distributed grids are used. Central difference schemes with second-order accuracy are then implemented.

For time integration, the vorticity field ω is updated at each time step by numerically integrating the vorticity equation (3) via an alternative direction implicit algorithm. Two boundary conditions are specified as following: at the outer boundary the vorticity goes to zero; the body-bound vorticity is obtained by expanding the stream function ψ in r direction near the body surface and incorporating the no-slip condition (8).

The Poisson equation (4) is solved using an efficient spectral-space method. To elaborate, both sides of the equation are expanded into N_θ Fourier modes with respect to θ. Owing to the linearity of the equation, the Fourier modes can be decoupled, leading to N_θ one-dimensional ordinary differential equations, which can be readily solved.

D. Validation of the Navier–Stokes solver

The validation of the Navier–Stokes solver developed above is conducted by comparing its predictions (both the hydrodynamic loads and the near-body flow field) with benchmark results from experiments.

We first consider a case when the foil has a fixed angle of attack α and compare the predicted lifting force with the experimental measurements by Dickinson and Gotz.[23] To match the experimental setup, we use a thin foil with $s/\lambda=0.025$ and $e=0$. The Reynolds number based upon the chord length is 192. Numerically, 150×256 grids are implemented in the computational domain. The value to be compared is the lifting coefficient at the early stage of wake development when the leading-edge vortex remains attached to the foil. As plotted in Fig. 2, it is clear that our numerical predictions are in good agreement with the experiment over the whole range of the angle of attack we consider ($\alpha\in[0°,90°]$).

The near-body flow field, including vortices shed from both the leading and the trailing edges, is also recorded. For comparison we choose the digital particle image velocimetry (DPIV) rendition of the flow filed around a heaving/pitching foil in a uniform flow U at a Reynolds number $R_e=1100$.[4] In this experiment, a foil undergoes a prescribed pitching motion $h(t)=h_0\sin(\Omega t)$, as well as a prescribed heaving motion $\alpha=\alpha_0\sin(\Omega t+\psi)$. In addition to the Reynolds number, the problem is also characterized by the Strouhal number $S_t=\Omega h_0/(\pi U)$. In Fig. 3 we draw the flow field at two combinations of kinematic parameters. The numerical results are obtained by using a foil with $s/\lambda=e/\lambda=0.05$. In both cases the DPIV measurements and the numerical predictions are parallel with each other. In this figure, and in all the vorticity contours that follow, the lighter areas correspond to counterclockwise vortices and the darker areas correspond to clockwise vortices.

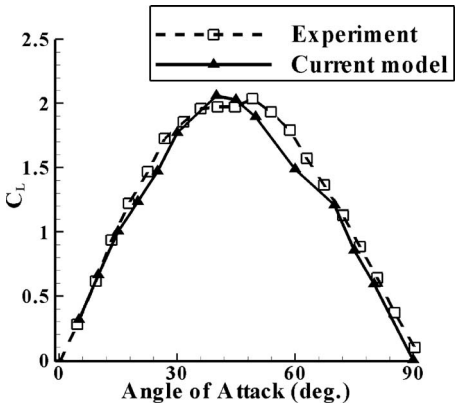

FIG. 2. Comparison of the lifting coefficient C_L on a fixed thin foil predicted by the Navier–Stokes model to the experimental measurements by Dickinson and Gotz (Ref. 23).

E. Fluid-structure interactions

Numerically, the coupling between the foil and its mounting system/energy generator (modeled by a damper), as expressed in Eq. (14) is achieved through an iteration algorithm. The major steps are as follows: (1) At time t, we start from an initial guess of the heaving motion $\dot{h}_1$ (usually prescribed as the value in the previous time step); (2) the hydrodynamic problem is solved based on $\dot{h}_1$; (3) the hydrodynamic lift F_L is calculated, from which the heaving speed $\dot{h}$ is obtained using Eq. (14); (4) If $\dot{h}$ is not sufficiently close

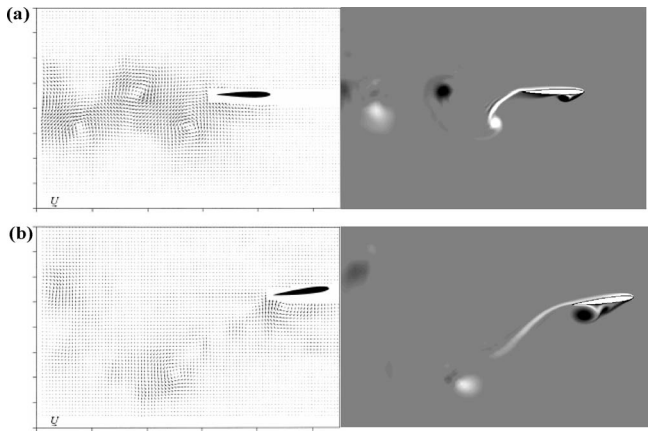

FIG. 3. Comparison between (left) DPIV measurements by Anderson *et al.* (Ref. 4) and (right) Navier–Stokes simulations by current model about the flow field around a foil undergoing sinusoidal heaving-pitching motions. The snapshots are taken when the foil is at its uppermost heaving position. The kinematic parameters are as follows: (a) $S_t=0.3$, $\alpha_0=15°$, $h_0/a=0.25$, $\psi=90°$; and (b) $S_t=0.36$, $\alpha_0=30°$, $h_0/a=0.75$, $\psi=75°$.

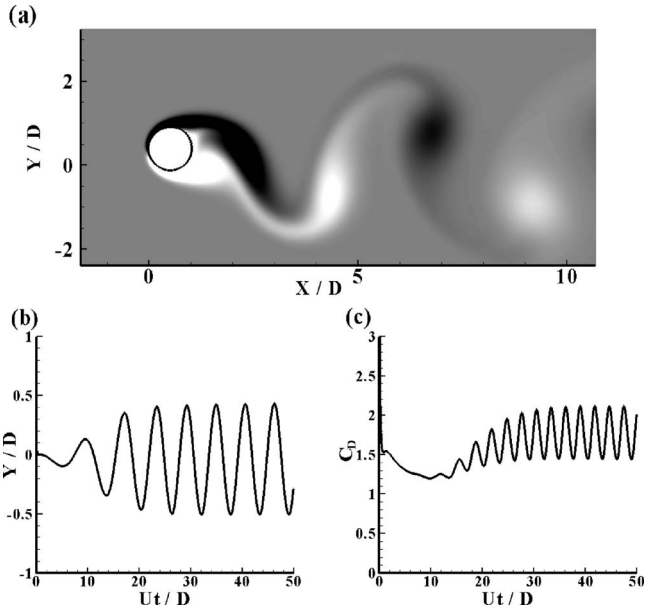

FIG. 4. (a) Near-body vorticity field, (b) transverse motion, and (c) drag coefficient of a circular cylinder in response to an incoming flow. $R_e=100$.

to $\dot{h}_1$, we set $\dot{h}_1=\dot{h}$ and repeat steps (2) and (3); (5) With the updated heaving speed, the new position of the foil h is obtained by integrating Eq. (14).

To eliminate the added-mass induced instability and improve the convergence of the aforementioned iteration algorithm, we apply an implicit added-mass method by subtracting the added-mass effects from both sides of Eq. (14) (see, e.g., Connell and Yue[24] and Zhu and Shoele[25]). As long as convergence of the iteration is achieved, the exact value of the added mass will not affect the results. In most cases, only (2) and (3) iteration steps are needed.

To demonstrate the accuracy of this fluid-structure interaction algorithm, we apply this method to simulate the fluid-induced vibration of a circular cylinder. The results are compared to predictions via the vortex method.[26,27] Within the framework of our formulation, the circular cylinder is approximately represented by setting $e=0$ and $s/\lambda \gg 1$ (in the following simulations we choose $s/\lambda=100$). Inside an incoming flow U, it is free to move in the transverse direction (without any mechanical restoring or damping) while its longitudinal position is fixed. To expedite the growth of instability, an initial disturbance in the form of a forced transverse motion with a maximum displacement of $0.03D$ (D is the diameter of the cylinder) is introduced within the time period of $t=0$ to $0.1D/U$. The cylinder is then released and its response is recorded. The outer boundary is about $50D$ away from the cylinder, and 250×256 grids are applied.

Figure 4 shows the near-body flow field as well as the transverse motion and the drag coefficient on the cylinder at $R_e=100$. The amplitude of motion is $0.47D$. This is close to the values predicted by Shiels *et al.*[26] ($0.46D$) and Eldredge and Pisani[8] ($0.45D$). The normalized frequency fD/U is 0.175 (compared to 0.156 in Ref. 26 and 0.148 in Ref. 8). The mean drag coefficient is 1.75 (compared to 1.73 in Ref. 26 and 1.66 in Ref. 8).

III. RESULTS

As indicated by our previous investigation utilizing a potential-flow based thin-plate model,[18] the energy harvesting capacity of a flapping-foil system is determined by its mechanical design (e.g., its chord length, location of the pitching axis, and the damping coefficient c) as well as kinematic parameters (e.g., the frequency of oscillation Ω and the pitching amplitude α_0). According to this simplified model, to achieve the sinusoidal pitching motion $\alpha(t)$, the mean power input of the system $\overline{P_i}$ is given as

$$\bar{P}_i' = -\sigma\alpha_0 \,\mathrm{Im}(M_0'), \tag{15}$$

where $\bar{P}_i'=\overline{P_i}/(\rho a U^3)$. Im is the operator to extract the imaginary part. $M_0'=M_0/(\rho a^2U^2)$. M_0 is a complex number with its magnitude being the amplitude of the hydrodynamic pitching moment on the plate (with respect to the pitching axis) and its phase the phase difference between the pitching motion and the moment. Since the system is assumed to be linear, the heaving response is also sinusoidal with amplitude h_0.

Using ρ, a, and U as normalization scales, we further define $\bar{P}_o'=\overline{P_o}/(\rho a U^3)$, $b'=b/a-1/2$, $h_0'=h_0/a$, $c'=c/(\rho a U)$, and the reduced frequency $\sigma=\Omega a/(2U)$.

By modeling the hydrodynamic effect as the combination of the quasisteady lifting force and pitching moment, the added-mass force and moment, and the adjustments due to wake formation, we have[19]

$$M_0' = \pi\{\sigma^2 b' h_0' - i\sigma(1/8 - b'/2)\alpha_0 + \sigma^2(1/32 + b'^2)\alpha_0 + C(\sigma)(b' - 1/4)[-2i\sigma h_0' + \alpha_0 + 2i\sigma(1/4 - b')\alpha_0]\}, \tag{16}$$

where $C(\sigma)$ is the deficiency factor representing effects of vorticity shedding from the trailing edge, which depends upon the reduced frequency σ. Mathematically, we have

$$C(\sigma) = \frac{K_1(i\sigma)}{K_0(i\sigma)+K_1(i\sigma)} = \frac{H_1^{(2)}(\sigma)}{H_1^{(2)}(\sigma)+H_0^{(2)}(\sigma)}, \tag{17}$$

where K_n $(n=0,1)$ is the modified Bessel function of the second kind, and $H_n^{(2)}$ $(n=0,1)$ is the Hankel function of the second kind.[19]

The heaving amplitude is expressed as[18]

$$h_0' = \left| \frac{\pi[1+2i\sigma(1/4-b')]C(\sigma) + \pi(i\sigma + 2b'\sigma^2)/2}{2i\sigma c' - \pi[-2i\sigma C(\sigma) + \sigma^2]}\alpha_0 \right|. \tag{18}$$

Thus the mean power output is

$$\bar{P}_o' = 2c'\sigma^2 h_0'^2. \tag{19}$$

As predicted by the model specified in Eqs. (15)–(19), in terms of the energy recovery capacity, the system performs better in lower frequencies than in higher frequencies. The maximum net power generation capacity has been identified as $P_m'=P_m/(\rho a U^3)=(\pi/8)\alpha_0^2$, achieved when σ is sufficiently small and $c'=\pi$.

Using this simplified model as guidance, instead of applying our Navier–Stokes model to map the performance of the system over the whole range of parameters (which is

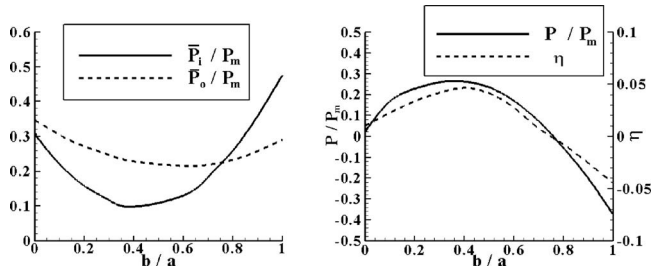

FIG. 5. Dependencies of the mean power input $\overline{P_i}$, the mean power output $\overline{P_o}$, the net power extraction P, and the efficiency η upon b, the location of the pitching axis. $\sigma=0.628$. $\alpha_0=15°$.

computationally infeasible), we concentrate in the vicinity of the region where high energy harvesting performance is observed. Specifically, we set $c'=\pi$, and study the effects of b, σ, and α_0. In all the cases, the geometry of the foil is set to be $s/\lambda=e/\lambda=0.05$. The Reynolds number R_e is 1000.

A. Effects of the mechanical and the kinematic parameters

In Fig. 5 we plot the Navier–Stokes prediction of the mean power input $\overline{P_i}$, the mean power output $\overline{P_o}$, the net power extraction P, and the efficiency η as functions of b, the location of the pitching axis. For other parameters, we choose the reduced frequency $\sigma=0.628$ and the pitching amplitude $\alpha_0=15°$. The results clearly show that both P and η reach their maxima near $b/a\sim0.3-0.4$ [Fig. 5(b)]. This is mostly attributed to the fact that $\overline{P_i}$ is greatly diminished near that region [Fig. 5(a)].

To interpret this, in Fig. 6 we plot the distribution of the pressure coefficient $C_p=p/(1/2)\rho U^2$ along the foil surface over half a period at $b=a/3$. It is seen that the peaks of the pressure usually appear close to the leading edge. It is therefore clear that when the pitching axis is located close to the peak pressure the system achieves optimal performance owing to the diminished hydrodynamic moment, and consequently the reduced power requirement for activation of the pitching motion. Similar conclusions have been drawn with other combinations of parameters.

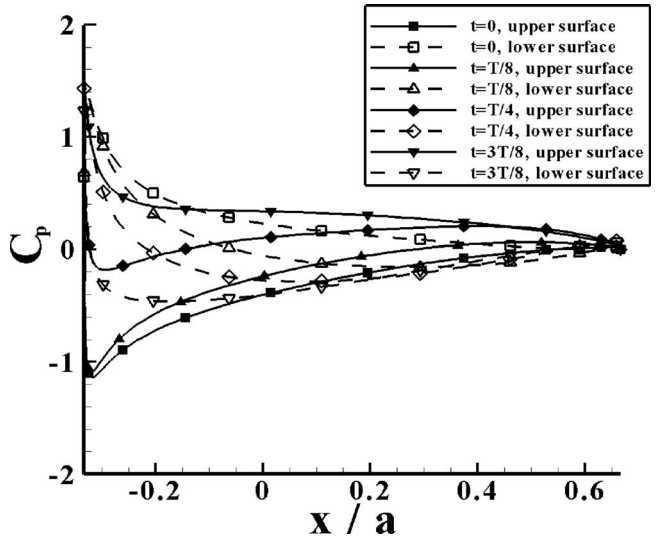

FIG. 6. Distribution of the pressure coefficient C_p on the foil surface.

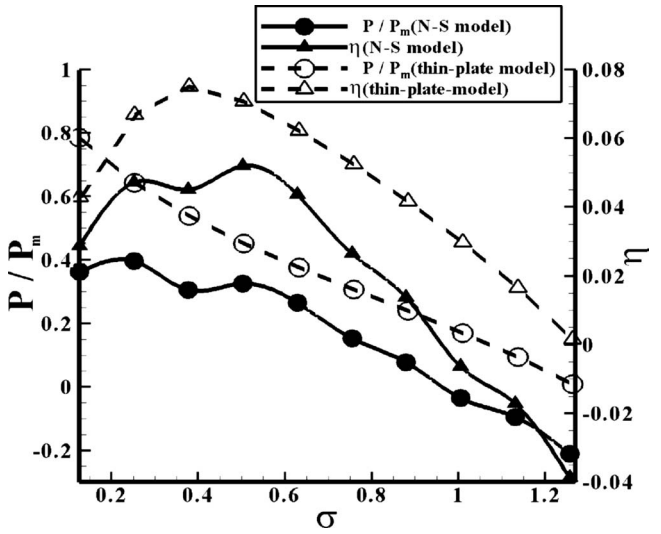

FIG. 7. The net power extraction P and the efficiency η as functions of the frequency.

Based upon this observation, we choose $b=a/3$ (i.e., the pitching axis is 1/3 chord from the leading edge) for the rest of the calculations.

Both the potential-flow model and the Navier–Stokes model show that the heaving amplitude h_0 increases as the frequency Ω decreases. Indeed, it is obvious that according to Eq. (18) as $\Omega\to0$, $h_0\to\infty$. Physically, this corresponds to the scenario of a steady lift force at a steady angle of attack. On the other hand, the relation between the power production and the frequency is not as clear owing to the fact that the power output is linearly proportional to the heaving speed. To numerically predict the dependence of P on Ω, we use an example with $\alpha_0=15°$ and plot P and η as functions of the reduced frequency σ (Fig. 7). It is seen that they reach peak values at $\sigma\sim0.4-0.7$. Moreover, as $\sigma>\sim0.9$, no positive energy extraction is achieved. For comparison, in the same figure we also plot results based on the thin-plate model summarized in Eqs. (15)–(19), which predicts higher values in both P and η.

According to the thin-plate model, the net power production P is quadratically proportional to the pitching amplitude α_0. Similarly, it has been found that the efficiency η is linearly proportional to α_0. These conclusions have also been confirmed by fully nonlinear simulations using a three-dimensional panel method.[18] These calculations, however, are based upon the potential-flow assumption and are therefore accurate only in infinitely large Reynolds numbers. Moreover, on the foil surface vorticity generation at locations other than the trailing edge is not included in the model. As illustrated in experiments (e.g., Ref. 4), when the frequency and/or the effective angle of attack are sufficiently high, the dynamics of a flapping foil is significantly affected by vortices shed from the leading-edge area. Thus, a Navier–Stokes simulation is essential in accurately predicting the mechani-

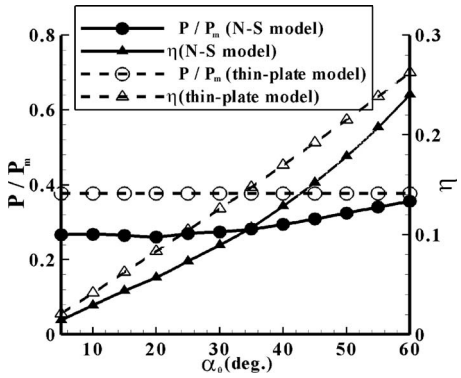

FIG. 8. The net power extraction P and the efficiency η as functions of the pitching angle.

cal behavior and energy harvesting capability of the flapping-foil system in large pitching angles where high performance is expected.

In Fig. 8 we plot the net power harvesting capacity P and the power extraction efficiency η as functions of α_0 as $\alpha_0 \in [5°, 60°]$ and $\sigma=0.628$. Within this range of α_0, P/P_m increases from 0.27 to 0.36, and η increases from 0.02 to 0.27. It is seen that the potential-flow prediction of P is higher than what is obtained by the Navier–Stokes model, while the Navier–Stokes predictions of P and η climb faster with increasing α_0. Within the range of α_0 the potential-flow model prediction of P/P_m is 0.38, surpassing the Navier–Stokes predictions by a margin from 41% (at $\alpha_0=5°$) to 6% (at $\alpha_0=60°$). The predictions of efficiency η by the two methods are closer to each other.

The discrepancies between the linearized potential-flow predictions and the Navier–Stokes predictions are caused by several mechanisms, including geometric nonlinearity (owing to the fact that the potential-flow model is formulated at the mean position of the foil), thickness effect, and viscous effect. In particular, with large pitching motions the foil generates vortices at the leading edge and this process is not included in the potential-flow approach. However, our simulations show that there may exist mechanisms to recover energy from the leading-edge vortices and diminish their effect on the overall energy exchange between the flow and the system. To investigate this, in the following we examine the near-body vorticity field and correlate it with the performance of the system.

B. Vorticity control mechanisms and LEV energy recovery

To study the correlation between the near-body flow field and the energy harvesting performance, we take a close-up examination of two representative cases, one with a small pitching amplitude ($\alpha_0=15°$) and the other with a large pitching amplitude ($\alpha_0=45°$). The oscillation frequency remains the same as the case studied above ($\sigma=0.628$).

In Fig. 9 we draw snapshots of the vorticity field around the foil at $\alpha_0=15°$ over half a period. The flow remains attached to the foil surface until it reaches the trailing edge. In addition, in the near field the wake vorticity is concentrated within a layer behind the foil. This scenario is reminiscent of

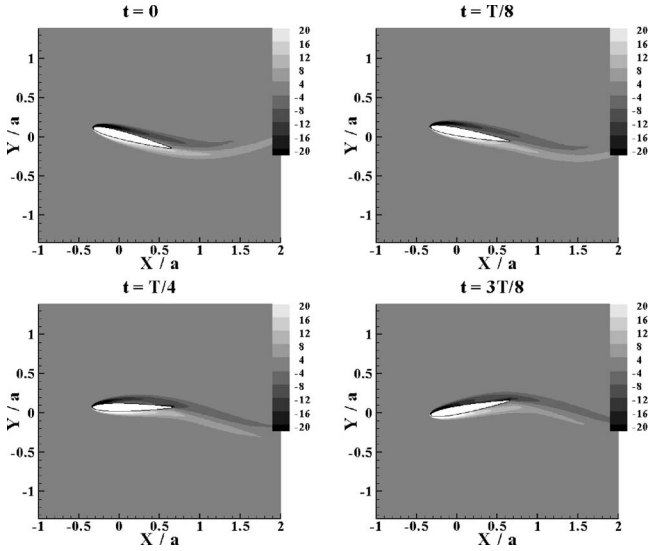

FIG. 9. The near-body vorticity fields over half a period with $\sigma=0.628$ and $\alpha_0=15°$. The value of the vorticity is normalized by U/a.

the potential-flow description, in which the wake is represented as a zero-thickness shear layer. Both the power input P_i and the power output P_o appear to be linearly correlated with the pitching movement $\alpha(t)$, with P_i positive over the whole period (Fig. 10).

A completely different behavior involving vortex-body interaction is observed in the case with a large pitching angle $\alpha_0=45°$. As shown in Fig. 11, vortices created near the leading edge interact with the rest part of the foil before reshedding into the wake (see the figure at $t\sim 3T/8$). A secondary vortex is induced by the LEV. Its strength, on the other hand, is not sufficient to have a significant effect on the evolution of the flow field (in contrast to the case with $\sigma=1.254$ as discussed below). When the LEV approaches the foil surface, it generates a region with low pressure. As displayed in Fig. 12(a), this distribution of low pressure occurs at the upper surface of the foil close to the trailing edge (located at $x/a=2/3$). In that figure, the peak of the negative pressure occurs at $x/a\sim 0.57$. Since the pitching axis locates at 1/3 chord from the leading edge ($x=0$), this low pressure near

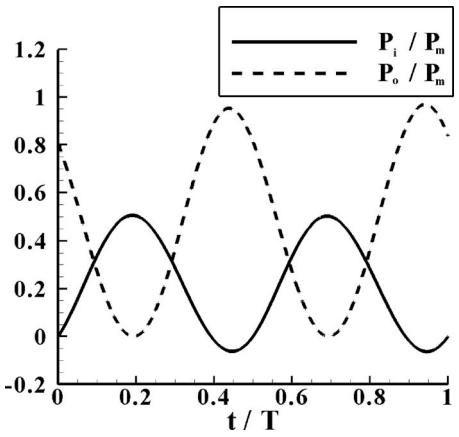

FIG. 10. Variations of the power input P_i and the power output P_o over one period. $\sigma=0.628$. $\alpha_0=15°$. The net power extraction $P/P_m=0.264$.

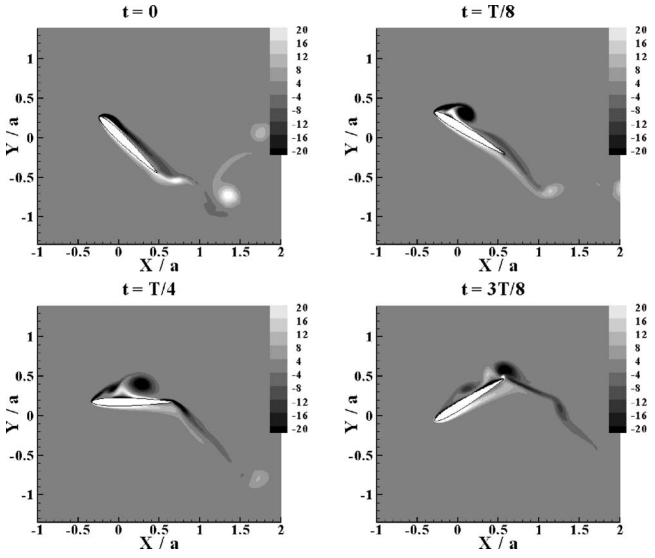

FIG. 11. The near-body vorticity fields over half a period with $\sigma=0.628$ and $\alpha_0=45°$. The value of the vorticity is normalized by U/a.

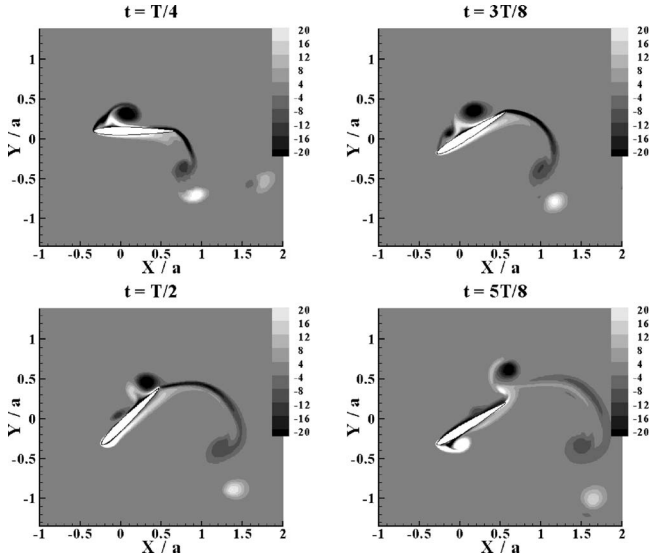

FIG. 13. The near-body vorticity fields over half a period with $\sigma=0.942$ and $\alpha_0=45°$. The value of the vorticity is normalized by U/a.

the trailing edge generates a counterclockwise pitching moment. The occurrence of this event coincides with the counterclockwise rotation of the foil, enabling energy transfer from the flow field into the system. This is clearly demonstrated in Fig. 12(b), where negative power input (i.e., energy gain) P_i is observed as $t\sim 0.35T$ and $t\sim 0.85T$, both coinciding with LEV-foil encounter. The low-pressure area stays with the foil even after its rotational direction is reversed, increasing the energy input during part of the period [e.g., at $t\sim 0.4T$ in Fig. 12(b)]. This additional energy input is, however, much smaller than the energy recovered. The vortex-body interaction mechanism therefore provides a measure of energy recovery from LEV.

Synchronization between the foil movements and the evolution of the near-body vorticity field, determined primarily by the reduced frequency σ, is key to the LEV energy recovery. A slightly different dynamic behavior is observed by increasing the frequency σ to 0.942 while keeping other parameters unchanged. As shown in Fig. 13, the LEV interacts with the foil and creates a secondary vortex as well as a low-pressure area on the foil surface [Fig. 14(a)], similar to the aforementioned scenario. The manner this LEV eventually detaches from the foil surface, on the other hand, is different from the previous case. As we see in Fig. 13, the LEV leaves the foil under the effect of the downward motion of the foil itself before the rotational direction of the foil is reversed. Thus, no additional energy consumption for the reshedding of the LEV is required, as displayed in Fig. 14(b).

In addition to the above-mentioned interaction scenarios between LEVs and the foil, other modes have also been identified. Specifically, we find that not all vortex-body interaction modes are beneficial to energy production. For illustration, in Fig. 15 we demonstrate the vorticity field around a foil with $\alpha_0=45°$ and $\sigma=1.254$. Interaction between the foil and a LEV occurs at $t\sim 0-T/8$, when the LEV induces a secondary vortex and forms a vortex pair. This does create a low-pressure distribution on the lower surface of the foil [Fig. 16(a) around $x/a\sim 0.25$]. However, the induced moment is small since the low-pressure area is close to the pitching axis at $x=0$. More importantly, the induced pitching moment is in the opposite direction of the instantaneous pitching motion. For these reasons, in this interaction mode no energy recovery from the LEV is obtained [Fig. 16(b)].

As LEVs stay close to the foil surface they can also

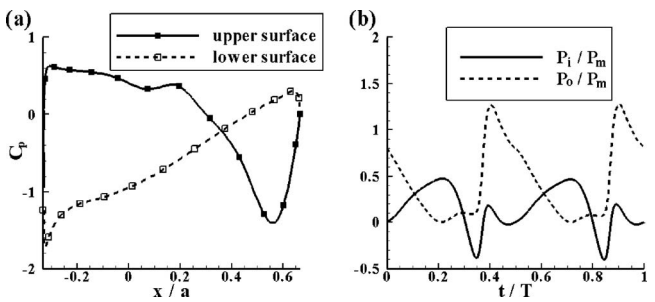

FIG. 12. (a) Distribution of the pressure coefficient on the foil surface at $t/T=0.35$. (b) Variations of the power input P_i and the power output P_o over one period. $\sigma=0.628$. $\alpha_0=45°$. The net power extraction $P/P_m=0.307$.

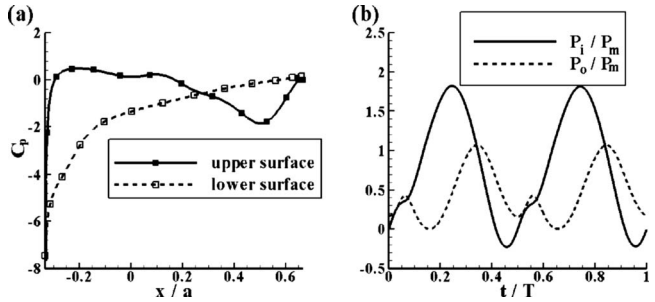

FIG. 14. (a) Distribution of the pressure coefficient on the foil surface at $t/T=0.47$. (b) Variations of the power input P_i and the power output P_o over one period. $\sigma=0.942$. $\alpha_0=45°$. The net power extraction $P/P_m=-0.344$.

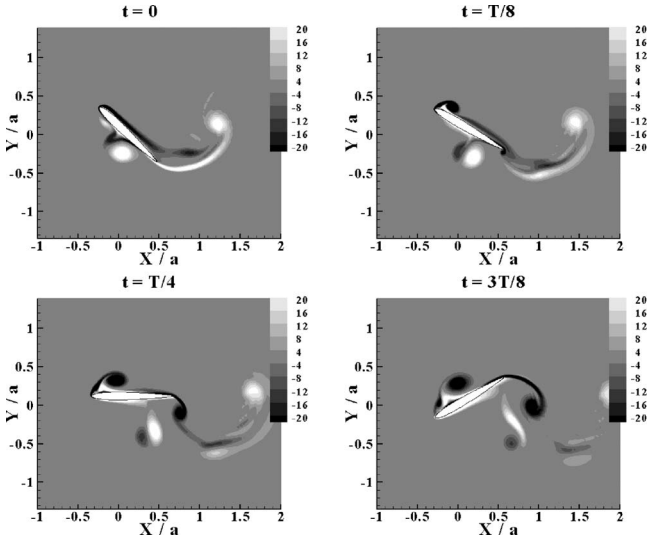

FIG. 15. The near-body vorticity fields over half a period with $\sigma=1.254$ and $\alpha_0=45°$. The value of the vorticity is normalized by U/a.

enhance the lifting force and may be beneficial to power generation.[17] This effect also depends upon the synchronization between the foil and the flow field.

IV. CONCLUSIONS

By using a fluid-structure interaction model based upon a finite-difference solver of the Navier–Stokes equations, we examined the physical process of energy extraction from a uniform flow through the coupling between pitching and heaving modes of a flapping foil in low Reynolds numbers. In this scenario, a periodic pitching motion is enforced, and energy recovery is rendered from the heaving motion that follows. For simplicity, the energy extraction process is idealized as a viscous damper. The overall energy recovery is the difference between the energy recovered from this damper and the energy input to create the pitching motion.

The performance of the foil-based flow energy harvesting system depends on mechanical parameters such as the magnitude of the damping and the location of the pitching axis, as well as operational parameters such as the frequency and amplitude of the pitching motion. Positive net energy extraction (i.e., the energy extracted is larger than the energy spent) is possible only in small frequencies. Our results show

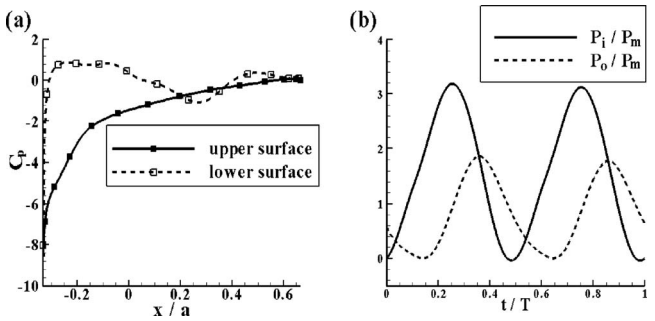

FIG. 16. (a) Distribution of the pressure coefficient on the foil surface at $t/T=0.35$. (b) Variations of the power input P_i and the power output P_o over one period. $\sigma=1.254$. $\alpha_0=45°$. The net power extraction $P/P_m=-0.813$.

that optimal performance is achieved when the pitching axis is close to the center of the hydrodynamic pressure so that the power input is minimized—in most cases a good choice is 0.2–0.5 chord length from the leading edge.

Vorticity control mechanisms, especially the interaction between the leading-edge vortices and the foil itself, play a critical role in the energy exchange between the foil and the surrounding flow field, and affect the performance of the system at large pitching angles. Specifically, we have identified an interaction mode in which part of the energy of the leading-edge vortices is recovered by the foil so that enhanced performance is obtained. To achieve this, two conditions have to be satisfied: (1) The energy recovery is obtained through the hydrodynamic moment induced by a LEV as it approaches the foil surface. This moment has to be in the same direction as the instantaneous pitching motion. (2) To maximize the moment it induces, the location of the vortex-foil encounter must be as far from the pitching axis as possible (ideally at the trailing edge).

Although our current model confirms that with the specific device the power harvesting capacity P cannot surpass P_m even if the mechanical design and the operational parameters are optimized, it is possible for further improvement through other measures. For example, our previous modeling based on potential flow shows that P can be significantly increased by utilizing ground effect, or by using two parallel foils in opposite phases of pitching. The inborn nonlinearity of the problem suggests that the dynamic behavior of the system might be different from what is illustrated in this study if the pitching motion is nonsinusoidal. This will bring in new parameters to be optimized. Indeed, nonsinusoidal pitching motions were applied in existing prototypes such as the Stingray as mentioned in the introduction. Clearly, further investigation in this issue is necessary.

ACKNOWLEDGMENTS

We would like to thank Dr. L. Guglielmini for discussions about the Navier–Stokes solver.

[1] M. S. Triantafyllou, A. H. Techet, and F. S. Hover, "Review of experimental work in biomimetic foils," IEEE J. Ocean. Eng. **29**, 585 (2004).
[2] R. Gopalkrishnan, M. S. Triantafyllou, G. S. Triantafyllou, and D. Barrett, "Active vorticity control in a shear flow using a flapping foil," J. Fluid Mech. **274**, 1 (1994).
[3] J. M. Anderson, "Vorticity control for efficient propulsion," Ph.D. thesis, Massachusetts Institute of Technology and the Woods Hole Oceanographic Institution, 1996.
[4] J. M. Anderson, K. Streitlien, D. S. Barrett, and M. S. Triantafyllou, "Oscillating foils of high propulsive efficiency," J. Fluid Mech. **360**, 41 (1998).
[5] Q. Zhu, M. Wolfgang, D. K. P. Yue, and M. S. Triantafyllou, "Three-dimensional flow structures and vorticity control in fish-like swimming," J. Fluid Mech. **468**, 1 (2002).
[6] J. C. Liao, D. N. Beal, G. V. Lauder, and M. S. Triantafyllou, "Fish exploiting vortices decrease muscle activity," Science **302**, 1566 (2003).
[7] J. Deng, X. M. Shao, and Z. S. Yu, "Hydrodynamic studies of two wavy foils in tandem arrangement," Phys. Fluids **19**, 113104 (2007).
[8] J. D. Eldredge and D. Pisani, "Passive propulsion of a simple articulated system in the wake of an obstacle," J. Fluid Mech. **607**, 279 (2008).
[9] H. Isshiki, M. Murakami, and Y. Terao, "Utilization of wave energy into propulsion of ships: Wave devouring propulsion," *15th Symposium on Naval Hydrodynamics* (National Academy, Washington, D.C., 1984), pp. 539–552.

[10]J. Grue, A. Mo, and E. Palm, "Propulsion of a foil moving in water waves," J. Fluid Mech. **186**, 393 (1988).
[11]W. McKinney and J. DeLaurier, "The wingmill: An oscillating-wing windmill," J. Energy **5**, 109 (1981).
[12]K.D. Jones and M.F. Platzer, "Numerical computation of flapping-wing propulsion and power extraction," presented at the 35th Aerospace Sciences Meeting and Exhibit, Reno, NV, 6–10 January 1997, AIAA Paper No. 97-0826.
[13]K. D. Jones, K. Lindsey, and M. F. Platzer, "An investigation of the fluid-structure interaction in an oscillating-wing micro-hydropower generator," *Fluid Structure Interaction II* (WIT, Southampton, UK, 2003), pp. 73–84.
[14]G. Dumas and T. Kinsey, "Eulerian simulations of oscillating airfoils in power extraction regime," in *Advances in Fluid Mechanics VI* (WIT, Southampton, UK, 2006), p. 245.
[15]A. Betz, *Introduction to the Theory of Flow Machines* (Pergamon, Oxford, 1966).
[16]A. Westwood, "Ocean power wave and tidal energy review," Refocus **5**, 50 (2004).
[17]E. Shimizu, K. Isogai, and S. Obayashi, "Multiobjective design study of a flapping wing power generator," ASME J. Fluids Eng. **130**, 021104 (2008).
[18]Q. Zhu, M. Haase, and C. H. Wu, "Modeling the capacity of a novel flow-energy harvester," Appl. Math. Model. **33**, 2207 (2009).
[19]T. Theodorsen, "General theory of aerodynamic instability and the mechanisms of flutter," National Advisory Committee for Aeronautics Report No. 496 (1935).
[20]L. Guglielmini and P. Blondeaux, "Propulsive efficiency of oscillating foils," Eur. J. Mech. B/Fluids **23**, 255 (2004).
[21]J. D. Eldredge, "Numerical simulation of the fluid dynamics of 2D rigid body motion with the vortex particle method," J. Comput. Phys. **221**, 626 (2007).
[22]Z. J. Wang, "Vortex shedding and frequency selection in flapping flight," J. Fluid Mech. **410**, 323 (2000).
[23]M. H. Dickinson and K. G. Gotz, "Unsteady aerodynamic performance of model wings at low Reynolds numbers," J. Exp. Biol. **174**, 45 (1993).
[24]B. S. H. Connell and D. K. P. Yue, "Flapping dynamics of a flag in a uniform stream," J. Fluid Mech. **581**, 33 (2007).
[25]Q. Zhu and K. Shoele, "Propulsion performance of a skeleton-strengthened fin," J. Exp. Biol. **211**, 2087 (2008).
[26]D. Shiels, A. Leonard, and A. Roshko, "Flow-induced vibration of a circular cylinder at limiting structural parameters," J. Fluids Struct. **15**, 3 (2001).
[27]J. D. Eldredge, "Dynamically coupled fluid-body interactions in vorticity-based numerical simulations," J. Comput. Phys. **227**, 9170 (2008).